PERGAMON

International Journal of Heat and Mass Transfer 43 (2000) 1603–1616

International Journal of HEAT and MASS TRANSFER

www.elsevier.com/locate/ijhmt

Computation of heat transfer in rotating two-pass square channels by a second-moment closure model

Hamn-Ching Chen[a], Yong-Jun Jang[b], Je-Chin Han[b,*]

[a]*Ocean Engineering Program, Department of Civil Engineering, Texas A & M University, College Station, TX, USA*
[b]*Turbine Heat Transfer Laboratory, Department of Mechanical Engineering, Texas A & M University, College Station, TX 77843, USA*

Received 16 February 1999; received in revised form 29 June 1999

Abstract

A multiblock numerical method has been employed for the calculation of three-dimensional flow and heat transfer in rotating two-pass square channels with smooth walls. The finite-analytic method solves Reynolds-averaged Navier–Stokes equations in conjunction with a near-wall second-order Reynolds stress (second-moment) closure model and a two-layer k–ε isotropic eddy viscosity model. Comparison of second-moment and two-layer calculations with experimental data clearly demonstrate that the secondary flows in rotating two-pass channels have been strongly influenced by the Reynolds stress anisotropy resulting from the Coriolis and centrifugal buoyancy forces as well as the 180° wall curvatures. The near-wall second-moment closure model provides accurate heat transfer predictions which agree well with measured data.

1. Introduction

Advanced gas turbine blades are subjected to high thermal stress due to increased turbine inlet temperature. Efficient internal convective cooling is required to maintain allowable blade temperatures and lengthen blade life. Characteristics of flow and local heat transfer in the cooling passages are important in the prediction of blade temperature and life. Some experimental and numerical studies have been conducted in this field. We restrict our review to turbulent flow and heat transfer studies in rotating coolant passages with smooth walls.

Wagner et al. [1] performed the most thorough experimental investigation on the effects of Coriolis and buoyancy forces on local heat transfer coefficient distributions of a multi-pass square channel with smooth walls. They suggested that differences in heat transfer between rotating and nonrotating flow conditions is primarily due to the secondary flows associated with Coriolis and centrifugal buoyancy forces. The local heat transfer coefficients on the trailing surface of the first coolant passage (radially-outward flow) increase with increasing rotational speed and wall-to-coolant temperature difference. However, the local heat transfer coefficients on the leading surface decrease with increasing rotational speed (up to $Ro = 0.24$) but increase with wall-to-coolant temperature differences. The heat transfer coefficient for the radially inward flowing passage increases on the leading surface and decreases on the trailing surface, which is the opposite of the effect in the outward flowing passage. Since Wagner et al. [1] experiments are very close to typical turbine blade

* Corresponding author. Tel.: +1-409-845-3738; fax: +1-409-862-2418.
E-mail address: jchan@mengr.tamu.edu (J.-C. Han).

0017-9310/00/$ - see front matter
PII: S0017-9310(99)00227-6

Nomenclature

D_h, D	hydraulic diameter	S	streamwise distance
h	heat transfer coefficient	T	local coolant temperature
K	thermal conductivity of coolant	T_o	coolant temperature at inlet
Nu	local Nusselt number, hD_h/K	T_w	wall temperature
Nu_o	Nusselt number in fully-developed turbulent nonrotating tube flow	W_b	bulk velocity in streamwise direction
		ρ	density of coolant
Pr	Prandtl number	$\Delta\rho/\rho$	coolant-to-wall density ratio, $(T_w-T_o)/T_w$
Re	Reynolds number, $\rho W_b D_h/\mu$	Ω	rotational speed
r_i	inner radius of bend	θ	dimensionless temperature, $(T-T_o)/(T_w-T_o)$
Ro	rotation number, $\Omega D_h/W_b$		
R_r	radius from axis of rotation	μ	dynamic viscosity of coolant

cooling conditions, their data has been used by various researchers as baseline comparisons.

Prakash and Zerkle [2] performed the numerical prediction of flow and heat transfer in a radially-outward rotating square duct. They employed the high-Reynolds-number version of the k–ε model with the wall function approximation. Their results indicated that the rotational buoyancy effects are significant under engine operating conditions. They also concluded that the high-Re k–ε turbulence model could not provide accurate heat transfer predictions and that more refined turbulence models should be used to get better results. Bo et al. [3] numerically predicted fully developed turbulent flow and heat transfer in a radially-outward rotating square (one-pass) duct. They used three turbulence models: a k–ε eddy viscosity model (EVM) with one equation in the near wall region, a low-Re k–ε eddy viscosity model, and a low-Re algebraic stress model (ASM). The k–ε/one-equation EVM produces reasonable heat transfer predictions, but some deficiencies emerge at the higher rotation number. In contrast, the low-Re k–ε EVM predictions showed unrealistic behavior, while the low-Re ASM results are close to the Wagner et al. [1] measurements. Dutta et al. [4] predicted the heat transfer from leading and trailing sides of a rotating square channel with radially outward flow (one-pass). They modeled terms for the Coriolis and buoyancy effects in the k–ε transport equations, that show better agreement with the Wagner et al. [1] experimental data.

Besserman and Tanrikut [5] calculated the flow and heat transfer in a stationary square duct with a 180° bend. They showed that the wall-function approach failed to accurately predict the heat transfer in high gradient regions whereas the predictions with wall integration provided better agreement with the measurements of Wagner et al. [1]. Sathyamurthy et al. [6] presented numerical results on the rotating square duct with a 180° bend (two-pass). The standard k–ε turbulence model with wall function treatment was adopted. They indicated that either a low Reynolds number k–ε model, two-layer k–ε model or second-moment closure model is needed for accurate prediction of flow and heat transfer for this complex flow situation. McGrath and Tse [7] performed the computation on the four pass, serpentine passage with three 180° turns which is identical to that of Wagner et al. [1] using the k–ε turbulence model with two wall treatments: the generalized wall function and the classical Van-Driest mixing length formulation. The two-layer wall integration turbulence model provides improvement over the wall function simulation. Stephens et al. [8] predicted the nature of the three-dimensional flow induced by Coriolis force, centrifugal buoyancy and a 180° bend in a rotating two-pass square duct with smooth walls. The computations were performed using a low Reynolds number k–ω model of turbulence and the computed heat transfer coefficient compared reasonably well with Wagner et al. [1] experimental data except for the leading surface in the first passage, where the heat transfer coefficients were overestimated by this model. Iacovides et al. [9] explored turbulence modeling issues related to duct flow influenced by strong curvature and rotation. They tested four turbulence models: the high-Re k–ε model with one-equation model in the near-wall regions, the high-Re algebraic second-moment (ASM) closure with one-equation near-wall model, the low-Re ASM model in which the dissipation rate of turbulence is obtained algebraically with the wall sublayers, and the low-Re ASM model in which the ε transport equation is solved over the entire domain. The computations of flow through a stationary 180° bend suggested that turbulence anisotropy within the duct core and the wall sublayer has a strong influence on the development of flow affected by strong curvature. In stationary case, the two low-Re ASM models

produced better predictions of the flow development than the other two turbulence models. In rotating case, however, the complex flow field downstream of the bend is not well reproduced by the low-*Re* ASM models (they did not consider the energy transport in the duct). Bonhoff et al. [10] presented the heat transfer predictions for rotating U-shaped coolant channels. The differential Reynolds stress model (RSM) was used for the calculation. The averaged heat transfer predictions were close to Wagner et al. [1] experimental results in the first passage of the channel, while the heat transfer in the second passage was overestimated by RSM.

None of the above-mentioned studies accurately predicted the flow and heat transfer behaviors in a rotating two-pass square duct with smooth walls under typical turbine blade cooling conditions. Particularly, accurate predictions in the 180° bend and in the second passage of the two-pass duct are lacking due to the unsophisticated turbulence closure models used. Therefore, there is a need to systematically evaluate the capability of using the second-moment closure model for accurate resolution of nonequilibrium turbulence produced by strong wall curvatures and rotational effects. This paper presents the prediction of flow characteristics and heat transfer results in a rotating square duct with a 180° bend which is the first two passages of the four-pass, serpentine passage that was experimentally investigated by Wagner et al. [1]. The computations were mainly performed by a near-wall second-moment turbulence closure model, while a two-layer k–ε eddy viscosity model was also included for comparison.

2. Governing equations

In the present study, calculations were performed for a rotating two-pass square channel using the near-wall second-order Reynolds stress closure model of Chen [11,12] and two-layer eddy viscosity model of Chen and Patel [13]. Both models were developed originally for incompressible flows in nonrotating coordinates. They have been generalized here to include the effects of rotation and buoyancy. For completeness, we shall summarize the generalized near-wall second-moment closure and the two-layer eddy viscosity model in the following:

2.1. Second-moment closure model

Consider the nondimensional Reynolds-averaged Navier–Stokes equations in general curvilinear coordinates (ξ^i, t), $i = 1, 2, 3$, for unsteady incompressible flow

$$\frac{\partial \rho}{\partial t} + (\rho U^m)_{,m} = 0 \tag{1}$$

$$\rho\left(\frac{\partial U^i}{\partial t} + U^m U^i_{,m} + R^{im}_{,m}\right) + 2\rho g^{il} e_{lmn}\Omega^m U^n + \rho g_{mn}(\Omega^i\Omega^m\xi^n - \Omega^m\Omega^n\xi^i) = -g^{im}p_{,m} + (\mu g^{mn}U^i_{,n})_{,m} \tag{2}$$

where e_{lmn} is the third-rank permutation tensor and Ω^m is the coordinate rotation vector. The metric tensor g_{mn} and conjugate metric tensor g^{mn} are given in Chen et al. [14]. $R^{im} = \overline{u^i u^m}$ is the Reynolds stress tensor. Overbars denote that the ensemble Reynolds averaging and the summation convention is used for repeated indices. The subscript, m represents the covariant derivative with respect to ξ^m. U^i and u^i are contravariant components of the mean and fluctuating velocities, t is time and p is pressure.

In the present study, the flow is considered incompressible since the Mach number is quite low. However, the density in the centrifugal force terms is approximated by $\rho = \rho_o T_o/T$ to account for the density variations caused by the temperature differences. ρ_o and T_o are the density and temperature at the inlet of the cooling channel.

The temperature T, is obtained from the energy equation

$$\rho c_p\left(\frac{\partial T}{\partial t} + U^m T_{,m} + \overline{u^m T'}\right) = g^{mn}(KT_{,n})_{,m} + \frac{Dp}{Dt} + \Phi \tag{3}$$

and Φ is the dissipation function defined by

$$\Phi = -\mu[U^m_{,n}U^n_{,m} + \overline{u^m_{,n}u^n_{,m}} + g_{ij}g^{mn}(U^i_{,m}U^j_{,n} + \overline{u^i_{,m}u^j_{,n}})] \tag{4}$$

where T and T' are the mean and fluctuating temperature fields, c_p is the specific heat at constant pressure, K is the thermal conductivity, and $\overline{u^m T'}$ is the kinematic turbulent heat flux.

The Reynolds stress tensor $R^{ij} = \overline{u^i u^j}$ is the solution of the transport equations

$$\frac{\partial R^{ij}}{\partial t} + U^m R^{ij}_{,m} = P^{ij} + D^{ij}_u + D^{ij}_p + D^{ij}_v + \Phi^{ij} - \varepsilon^{ij} \tag{5}$$

where

production

$$P^{ij} = -(R^{im}U^j_{,m} + R^{jm}U^i_{,m}) - 2e_{lmn}\Omega^m(g^{il}R^{jn} + g^{jl}R^{in})$$

diffusion by u^m $D^{ij}_u = -(\overline{u^i u^j u^m})_{,m}$

diffusion by p' $D_p^{ij} = -g^{jm}(\overline{u^i p'/\rho})_{,m} - g^{im}(\overline{u^j p'/\rho})_{,m}$

viscous diffusion $D_v^{ij} = \nu g^{mn} R^{ij}_{,mn}$

pressure–strain $\Phi^{ij} = \overline{(p'/\rho)(g^{im}u^j_{,m} + g^{jm}u^i_{,m})}$

and dissipation $\varepsilon^{ij} = 2\nu g^{mn}\overline{u^i_{,m}u^j_{,n}}$

.

To solve these equations, appropriate closure models must be provided for the pressure–strain, diffusion and dissipation terms. In the present study, the pressure–strain correlation of Speziale et al. [15] was combined with the near-wall Reynolds stress closure of Chen [11,12] for detailed resolution of three-dimensional boundary layer flow all the way up to the solid walls. For the sake of completeness, we will briefly summarize the present near-wall second-moment closure model in the following:

1. *Diffusion* $D^{ij} = D_u^{ij} + D_p^{ij}$ (Daly and Harlow [16])

$$D^{ij} = C_s'\left(\frac{k}{\varepsilon}R^{mn}R^{ij}_{,m}\right)_{,m}; C_s' = 0.22 \tag{6}$$

2. *Pressure–strain and dissipation* $\Phi^{ij}-\varepsilon^{ij}$ (Speziale et al. [15]; Chen [11,12])

$$\Phi^{ij} - \varepsilon^{ij} = \bar{\Phi}_1^{ij} + \Phi_2^{ij} + \Phi_w^{ij} - \tfrac{2}{3}g^{ij}\varepsilon \tag{7}$$

where

$$\begin{aligned}\bar{\Phi}_1^{ij} &= -\bar{C}_1\{1-(1-1/\bar{C}_1)f_w\}\varepsilon b^{ij} \\ &\quad + C_2(1-f_w)\varepsilon(g_{mn}b^{im}b^{jn} - \tfrac{1}{3}g^{ij}\mathrm{II})\end{aligned} \tag{8}$$

$$\begin{aligned}\Phi_2^{ij} &= (C_3 - C_3^*\mathrm{II}^{1/2})kS^{ij} + C_4k(g_{mn}b^{im}S^{jn} \\ &\quad + g_{mn}b^{jm}S^{in} - \tfrac{2}{3}g^{ij}g_{mr}g_{ns}b^{mn}S^{rs}) \\ &\quad + C_5k(g_{mn}b^{im}W^{jn} + g_{mn}b^{jm}W^{in})\end{aligned} \tag{9}$$

$$\begin{aligned}\Phi_w^{ij} &= f_w\{0.45(P^{ij} - \tfrac{2}{3}g^{ij}P) - 0.03(Q^{ij} - \tfrac{2}{3}g^{ij}P) \\ &\quad + 0.08k(2S^{ij})\}\end{aligned} \tag{10}$$

$$b^{ij} = \frac{R^{ij}}{2k} - \frac{1}{3}g^{ij}; \quad \mathrm{II} = g_{mr}g_{ns}b^{mn}b^{rs} \tag{11}$$

$$\begin{aligned}S^{ij} &= \tfrac{1}{2}(g^{jm}U^i_{,m} + g^{im}U^j_{,m}); \\ W^{ij} &= \tfrac{1}{2}(g^{jm}U^i_{,m} - g^{im}U^j_{,m})\end{aligned} \tag{12}$$

$$P = \tfrac{1}{2}g_{mn}P^{mn}; \quad Q^{ij} = -g_{lm}(g^{in}R^{jl} + g^{jn}R^{il})U^m_{,n} \tag{13}$$

$$\begin{aligned}\bar{C}_1 &= C_1 + C_1^*\frac{P}{\varepsilon}; \\ f_w &= \exp[-(0.0184Re\sqrt{k}y)^4],\end{aligned} \tag{14}$$

where the model coefficients $(C_1, C_1^*, C_2, C_3, C_3^*, C_4, C_5)$ are equal to respectively 3.4, 1.80, 4.2, 0.8, 1.30, 1.25, 0.40. It should be remarked here that the coefficient in f_w was adjusted from 0.015 to 0.0184 based on the numerical optimizations for the present test cases. Although the original coefficient of 0.015 worked well for high Reynolds number flows considered in Chen [12], it was found to produce too much damping effects for the low Reynolds number flows considered here. The new coefficient reduces the extent of the near-wall damping zone and is more consistent with the two-layer k–ε results. It is also worthwhile to note that the effects of the damping function f_w diminishes exponentially away from the solid surfaces with $\Phi_w^{ij} = 0$ in the fully turbulent regions. Therefore, the present near-wall Reynolds stress model automatically recovers the high-*Re* SSG second-moment closure of Speziale et al. [15] in the far-field. A more detailed description of the present near-wall second-moment closure is given in Chen [11,12].

In general, the turbulent heat fluxes $\overline{u^m T'}$ may also be solved directly using second-order closure models such as those shown in Launder [17]. In the current study, however, we will use the generalized gradient diffusion hypothesis (GGDH) given in Bo et al. [3]

$$\overline{u^m T'} = -C_\theta\frac{k}{\varepsilon}R^{mn}T_{,n}; \quad C_\theta = 0.225 \tag{15}$$

It should be noted that the C_θ value used here is somewhat lower than that proposed by Bo et al. [3] based on extensive numerical optimizations performed in the present calculations.

To complete the Reynolds stress closure, the rate of turbulent kinetic energy dissipation ε must also be modeled. In the present study, the low Reynolds number model of Chen [12] was adopted as follows:

$$\begin{aligned}\frac{\partial\varepsilon}{\partial t} + U^m\varepsilon_{,m} &= \{(\nu g^{mn} + C_\varepsilon\frac{k}{\varepsilon}R^{mn})\varepsilon_{,n}\}_{,m} \\ &\quad + C_{\varepsilon1}(1 + C_{\varepsilon4}f_w)\frac{\varepsilon}{k}P - C_{\varepsilon2}f_\varepsilon\frac{\varepsilon\varepsilon^*}{k} + \xi\end{aligned} \tag{16}$$

where the model coefficients are $(C_\varepsilon, C_{\varepsilon1}, C_{\varepsilon2}, C_{\varepsilon4}) = (0.15, 1.35, 1.8, 1.0)$. The near-wall damping function f_w, f_ε and the source terms ξ and ε^* are given in Chen [11,12].

2.2. Two-layer k–ε model

In order to facilitate a detailed assessment of the present near-wall second-order Reynolds stress closure for turbulent flow and heat transfer predictions, calculations were also performed using the two-layer isotropic eddy viscosity model of Chen and Patel [13]. In this two-layer approach, the Reynolds stresses are related to the mean rate of strain by

$$-\rho R^{ij} = 2\mu_t S^{ij} - \tfrac{2}{3} g^{ij}\rho k, \tag{17}$$

where μ_t is the eddy viscosity and $k = g_{ij}\overline{u^i u^j}/2$ is the turbulent kinetic energy. S^{ij} is the contravariant components of the rate of strain tensor given in Eq. (12). Similarly, the turbulent heat fluxes can be related to the mean temperature gradient as follows:

$$-\rho\overline{u^m T'} = \frac{\mu_t}{Pr_t} g^{mn} T_{,n} Pr_t = 0.9, \tag{18}$$

where Pr_t is the turbulent Prandtl number. Substitution into (2) and (3) yields momentum and energy equations for eddy viscosity turbulence modeling

$$\begin{aligned}&\rho\left(\frac{\partial U^i}{\partial t} + U^m U^i_{,m}\right) + \rho g^{il} e_{lmn}\Omega^m U^n \\ &+ \rho g_{mn}(\Omega^i\Omega^m\xi^n - \Omega^m\Omega^n\xi^i) \\ &= -g^{im}\left(p + \tfrac{2}{3}\rho k\right)_{,m} + 2\mu_{t,m} S^{im} \\ &+ (\mu + \mu_t) g^{mn} U^i_{,mn}\end{aligned} \tag{19}$$

$$\rho\left(\frac{\partial T}{\partial t} + U^m T_{,m}\right) = g^{mn}\left\{\left(\frac{\mu}{Pr} + \frac{\mu_t}{Pr_t}\right) T_{,n}\right\}_{,m} \tag{20}$$

where Pr is the Prandtl number. Eqs. (19) and (20) are closed using the two-layer turbulence model of Chen and Patel [13]. The approach utilizes a two-equation k–ε model for most of the flow field, but a one-equation k–l model in the viscous sublayer and buffer zone. The prescribed length scale (l) circumvents numerical problems often encountered with near-wall dissipation calculations and reproduces the universal law-of-the-wall profiles in the laminar sublayer, buffer layer and logarithmic regions.

In the fully turbulent region, the conservation equations for turbulent kinetic energy and its dissipation rate can be written:

$$\rho\left(\frac{\partial k}{\partial t} + U^m k_{,m}\right) = g^{mn}\left\{\left(\mu + \frac{\mu_t}{\sigma_k}\right) k_{,n}\right\}_{,m} + P + P_b - \rho\varepsilon \tag{21}$$

$$\rho\left(\frac{\partial \varepsilon}{\partial t} + U^m \varepsilon_{,m}\right) = g^{mn}\left\{\left(\mu + \frac{\mu_t}{\sigma_\varepsilon}\right)\varepsilon_{,n}\right\}_{,m} + \frac{\varepsilon}{k}(C_{\varepsilon 1} P + C_{\varepsilon 3} P_b - C_{\varepsilon 2}\rho\varepsilon) \tag{22}$$

where

$$P = 2 g_{np}\mu_t S^{mn} U^p_{,m} \tag{23}$$

$$P_b = \frac{\mu_t}{Pr_t T} g_{mn}(\Omega^m\Omega^l\xi^n - \Omega^m\Omega^n\xi^l) T_{,l} \tag{24}$$

The buoyancy generated turbulence production P_b was proposed by Snider and Andrews [18] and the model coefficients (C_μ, $C_{\varepsilon 1}$, $C_{\varepsilon 2}$, $C_{\varepsilon 3}$, σ_k, σ_ε) are fixed constants equal to 0.09, 1.44, 1.92, 0.9, 1.0, 1.3, respectively.

In the near-wall region, the rate of turbulent dissipation is specified in terms of k rather than being computed from (22). From Chen and Patel [13]:

$$\varepsilon = \frac{k^{3/2}}{\ell_\varepsilon} \tag{25}$$

where ℓ_ε is a dissipation length scale given by

$$\ell_\varepsilon = C_\ell y[1 - \exp(-R_y/A_\varepsilon)]; \quad R_y = \sqrt{k}y/\nu \tag{26}$$

With k and ε known, the eddy viscosity is found from

$$\nu_t = C_\mu\sqrt{k}\ell_\mu, \quad \ell_\mu = C_l y[1 - \exp(-R_y/A_\mu)] \tag{27}$$

The constants C_ℓ, A_μ and A_ε are chosen to yield a smooth distribution of eddy viscosity between the two regions, and take the values ($C_\ell = 0.418 C_\mu^{-3/4}$, $A_\mu = 70$, $A_\varepsilon = 2C_\ell$). A more detailed description of the two-layer model is given in Chen and Patel [13].

3. Chimera RANS method

In the present study, the chimera RANS method of Chen [11,12] and Chen and Chen [19] has been further extended to include the effects of rotation and buoyancy. The present method solves the mean flow and turbulence quantities in arbitrary combination of embedded, overlapped, or matched grids using a chimera domain decomposition approach. In this approach, the solution domain is first decomposed into a number of smaller blocks which facilitate efficient adaption of different block geometries, flow solvers and boundary conditions for calculations involving complex configurations and flow conditions. Within each computational block, the finite-analytic numerical method of Chen and Chen [20] and Chen et al. [14] was employed to solve the unsteady RANS

equations on a general curvilinear, body-fitted coordinate system. The coupling between the pressure and velocity is accomplished using a hybrid PISO/SIMPLER algorithm given in Chen and Patel [21] and Chen and Korpus [22]. The method satisfies continuity of mass by requiring the contravariant velocities to have a vanishing divergence at each time step. Pressure is solved using the concept of pseudo-velocities, and when combined with the finite-analytic discretization gives the Poisson equation for pressure. To ensure the proper conservation of mass and momentum between linking grid blocks, the grid-interface conservation techniques of Hubbard and Chen [23] and Chen and Chen [19] were employed to eliminate unphysical mass source resulting from the interpolation errors between the chimera grid blocks. More detailed descriptions of the chimera RANS method were given in Chen and Huang [24] and Chen and Liu [25].

4. Results and discussion

Calculations were performed for the multi-pass square channel with smooth walls as tested by Wagner et al. [1]. Fig. 1 shows the geometry and an enlarged view of the numerical grids around the 180° bend. Two of the four side walls in the rotation direction are denoted as the leading and the trailing surfaces, respectively. The other two side walls are denoted the inner and the outer surfaces. The length of both the first pass and second pass are $14D_h$. The inner radius

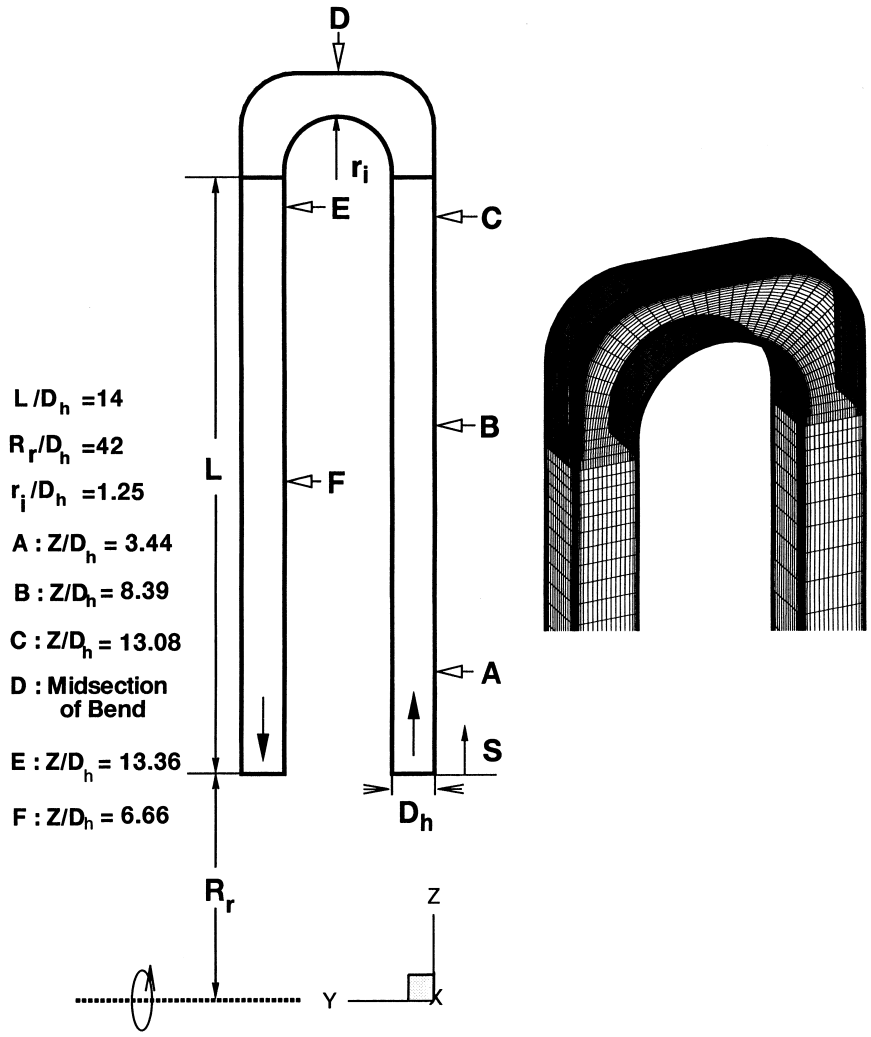

Fig. 1. Geometry and numerical grids.

of curvature of the bend is $1.25D_h$ and the radius from axis of rotation is $42D_h$. All walls are heated to a constant temperature. In this paper, the Reynolds number was fixed at 25,000 which is the typical operating conditions of medium size gas turbines. Comparisons between the calculations and measurements were made for three different rotation numbers of 0, 0.18 and 0.24, and four coolant-to-wall density ratios of 0, 0.07, 0.13 and 0.22. The Nusselt numbers presented herein were normalized with a smooth tube correlation (Kays and Crawford [26]) for fully developed, nonrotating, turbulent flow

$$Nu_o = 0.0176Re^{0.8} \tag{28}$$

The present numerical grid was generated using an interactive gridding code GRIDGEN developed by Steinbrenner et al. [27]. It was then reblocked into several interlocked computational blocks to facilitate the implementation of near-wall turbulence models and specification of boundary conditions. To provide adequate resolutions of the viscous sublayer and buffer layer adjacent to a solid surface, the minimum grid spacing in the near-wall region is maintained at 10^{-4} of the body length which corresponds to a wall coordinate y^+ of the order of 0.1. In all calculations, the root-mean-square (rms) and maximum absolute errors for both the mean flow and turbulence quantities were monitored for each computational block to ensure complete convergence of the numerical solutions. A convergence criterion of 10^{-5} was used for the maximum rms error in all computational blocks. In all cases, the computer CPU time required for the second-moment closure model is about twice of that for the two-layer eddy viscosity model.

In the present calculations, a fully-developed turbulent boundary layer profile was used at the entrance of the duct. Since the fully-developed profiles for mean flow and turbulence quantities are not known analytically, a separate calculation was performed for a straight duct to provide the inlet conditions at the duct entrance. At the exit of the duct, the flow was assumed to be parabolic with zero-gradient boundary conditions for mean velocity and all turbulence quantities, while linear extrapolation was used for the pressure field. The coolant temperature was T_o (i.e., $\theta=(T-T_o)/(T_w-T_o)=0$) at the entrance of the duct and the wall temperature was kept constant at $T=T_w$ ($\theta=1$) on all side walls.

A grid-refinement study was performed using four different grid distributions of $41\times41\times111$, $41\times41\times175$, $61\times61\times111$ and $81\times81\times111$ with the implementation of a general Chimera domain decomposition technique (Hubbard and Chen [23]; Chen and Chen [19]). The grid refinement in the axial direction has produced only minor changes in the bend region. Fig. 2 shows a comparison of the calculated Nusselt numbers on the leading surface ($Ro=0.24$, $\Delta\rho/\rho=0.13$) for $41\times41\times111$, $61\times61\times111$ and $81\times81\times111$ grid distribution with two-layer and second-moment models. In the two-layer model, the Nusselt number in the bend was improved by 9 and 15% respectively with $61\times61\times111$ and $81\times81\times111$ grids. The Nusselt number, however, was not significantly changed in the second-moment results except for the turning section where a 10% improvement was observed. All the results presented in the following discussions are based on an $81\times81\times111$ grid for the two-layer model and an $41\times41\times111$ grid for the second-moment model.

4.1. Velocity and temperature fields

The velocity, temperature fields and side-averaged Nusselt numbers for both the nonrotating and rotating square duct with 180° bend are presented in this section. For the sake of brevity, we shall present only the details of the three-dimensional velocity and temperature fields for the second-moment solutions since the second-order Reynolds stress model produced more accurate results for all test cases considered. The two-layer k–ε results will be discussed only in the comparison of Nusselt number distributions to quantify the effects of the Reynolds stress anisotropy.

Figure 3 shows the calculated secondary flow vectors and temperature contours at several axial stations defined in Fig. 1 for the nonrotating case. It is seen from Fig. 3C that the anisotropy of the turbulent Reynolds stresses produced small secondary corner vortices in the first passage. In the bend, the centrifugal forces and the associated pressure gradients (low pressure at inner surface, high pressure at outer surface) produced two counter-rotating vortices as shown in Fig. 3D which convected fluid from the core toward the outer

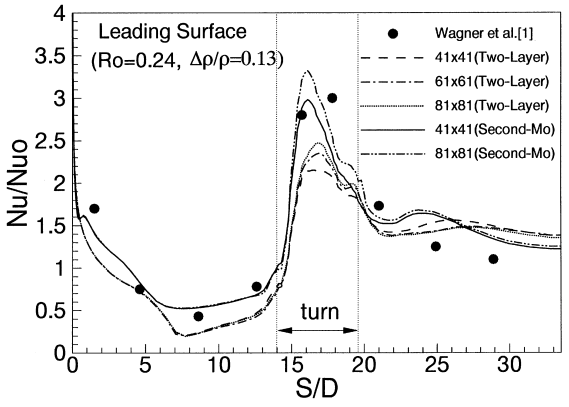

Fig. 2. Grid refinement study; Re = 25,000.

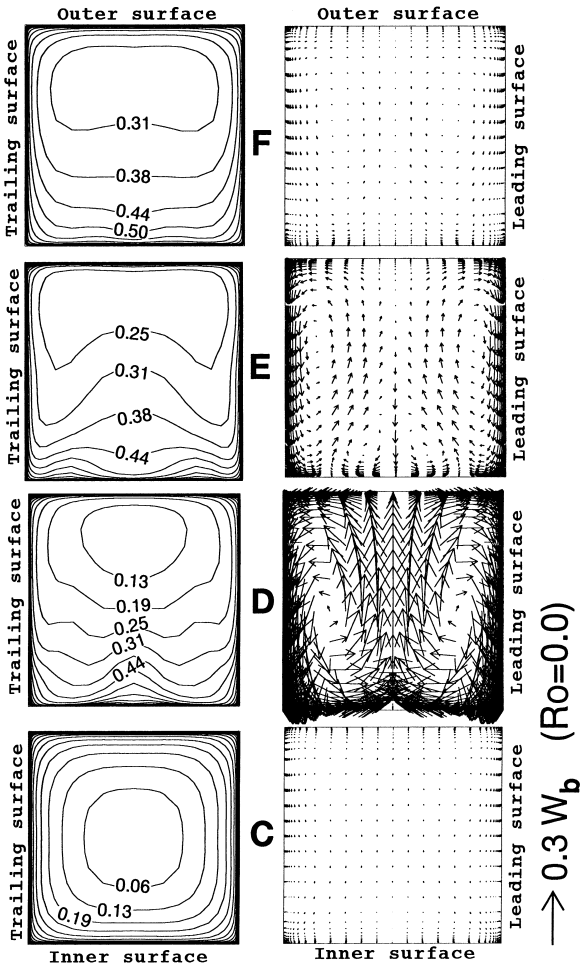

Fig. 3. Dimensionless temperature ($\theta=(T-T_o)/(T_w-T_o)$) and secondary-flows for nonrotating duct.

surface. This secondary flow started to decrease in the second passage and vanished almost completely at the end of the second passage. The left column of Fig. 3 shows the isothermal contours in the duct. Before the bend, the cooler fluids are located in the core region (Fig. 3C). After the bend, however, the cooler fluid is pushed toward the outer surface by the centrifugal force induced by the streamline curvatures. This leads to steep temperature gradients and hence high heat transfer coefficients on the outer wall after the bend as shown in Fig. 3D–F.

Figure 4 shows the cross-stream velocity vectors and the isothermal contours for the rotating case at selected planes of $Z/D_h=3.44$, 8.39, 13.08 (locations A, B and C in Fig. 1) in the first passage, location D in the bend and $Z/D_h=13.36$, 6.66 (locations E and F) in the second passage. In the first passage, the Coriolis forces produce a cross-stream flow pattern which pushes the cold fluid from the core towards the trailing surface and then returns along the side walls (i.e., inner and outer surfaces) where the fluid is heated. The secondary flow induced by the Coriolis forces also dis-

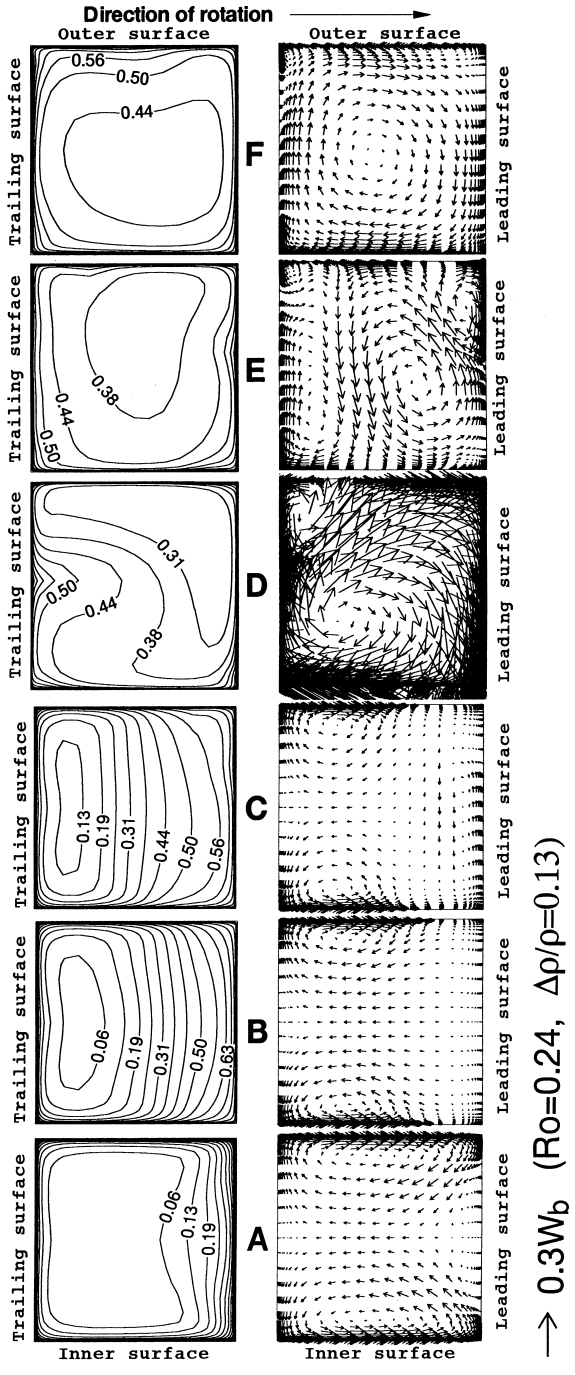

Fig. 4. Dimensionless temperature ($\theta=(T-T_o)/(T_w-T_o)$) and secondary-flow for rotating duct.

torts the axial velocity profiles. Initially a two-vortex secondary flow is formed near the inlet of the duct. After about 3.4 diameters of flow development, an extra pair of counter-rotating vortices is observed along the leading surface as shown in Fig. 4A. Farther downstream, the two vortex structure is again reestablished (Fig. 4B). This transient entry phenomenon is also predicted by the present two-layer eddy viscosity model, but the location of appearance of the four-vortex pattern was farther downstream than that predicted by the second moment closure model.

In the bend, the secondary flow structure formed in the first passage is completely destroyed as shown in Fig. 4D. The rotation-induced radially outward flow, as it enters the bend section of the duct, is accelerated asymmetrically in the cross section. The heavier cold fluid near the trailing surface is first accelerated and then followed by the lighter fluid near the leading surface in the duct cross section. This causes the fluid near the trailing surface to be thrown towards the outer side wall, resulting in the clockwise circulation in the middle of the bend region.

In the second passage, the Coriolis force acts in the opposite direction, compared to the one in the first passage, which pushes the cold fluid towards the leading surface. Fig. 4E shows the formation of two large vortices with the larger one near the leading surface and the smaller one near the trailing surface. This secondary flow structure is produced by the interaction of the circulation generated in the bend and the Coriolis force due to the duct rotation. Farther downstream at location 4-F, the peak crossflow velocities are still as high as 9% of W_b. The secondary flow at this station is caused primarily by the Coriolis force as the effect of bend diminishes gradually in the second passage.

For the nonrotating case, the computed axial velocity profiles (not shown) shift toward the outer surface in the bend, but return quickly to a fairly flat profile in the second passage. A detailed examination of the solutions reveals no axial flow reversal in this stationary duct. For the rotating case, the Coriolis forces push the cold fluids toward the trailing surface so that the centrifugal buoyancy force tends to slow down the lighter fluid, producing a thicker boundary layer near the leading surface and accelerates the heavier fluid near the trailing surface. Thus, it causes flow reversal in the streamwise direction on the leading surface. In general, the reverse flow region in the first passage increases with increasing coolant-to-wall density ratio and buoyancy. On the other hand, the Coriolis force in the second passage acts in the opposite direction and pushes the cold fluids toward the leading surface. Thus, the centrifugal buoyancy forces accelerate the lighter fluid near the trailing surface and, consequently, flatten the axial velocity profile. The effects of the above axial and secondary flow developments on the surface heat transfer will be presented in the following section.

4.2. Surface heat transfer

Figure 5a shows the Nu/Nu_o contour plots on the leading and trailing surfaces for the stationary case. For the first passage, the heat transfer is high near the inlet due to the thinner thermal boundary layers. Downstream, the heat transfer coefficient decreases and asymptotically approaches the fully developed value. The heat transfer in the bend and the outer surface of the second passage is high due to the secondary flows induced by the high pressure gradient in the bend.

Figure 5b and c show the Nu/Nu_o contours on the leading and trailing surfaces for rotating cases. On the leading surface, the Nusselt number reaches minimum in the middle of the first passage and increases significantly along the outer surface in the bend and also in the second passage of the duct. For the trailing surface, the Nusselt number increases sharply in the streamwise direction and reaches a maximum value in the bend region. In the second passage, the Nusselt number decreases gradually along the duct.

The side-averaged (along the spanwise direction) Nusselt number ratios on all four walls are shown in Fig. 6. Comparisons were made between the calculations and the experimental data of Wagner et al. [1]. The numerical results obtained from both the second-order Reynolds stress closure and two-layer eddy viscosity models are presented to facilitate a detailed assessment on the effects of the Reynolds stress anisotropy. For completeness, the numerical results by Bonhoff et al. [10] using a different Reynolds stress model with the wall function approach in the FLUENT code are also plotted in the same figures.

On the leading surface, the Nusselt number ratio for the second-moment closure model decreases initially up to $S/D = 7$ (this location is close to the measured data at $S/D = 8.5$) and then increases further downstream. The reason for this Nusselt number decrease is due to the thickening of the boundary layer caused by the Coriolis force effects. The subsequent increase in Nusselt number ratio is attributed to the centrifugal buoyancy induced reversed flow destabilized near-wall turbulence boundary layer. The Nusselt number ratio on the trailing surface decreases sharply near the duct entrance and then increase continuously in the first passage. The higher Nusselt numbers on the trailing surface are caused by the Coriolis force pushing the cooler fluid toward the trailing surface which creates a thinner boundary layer on that side. In the bend section, the Nusselt numbers increase on all four side walls. These increases are due to the mixing of cooler

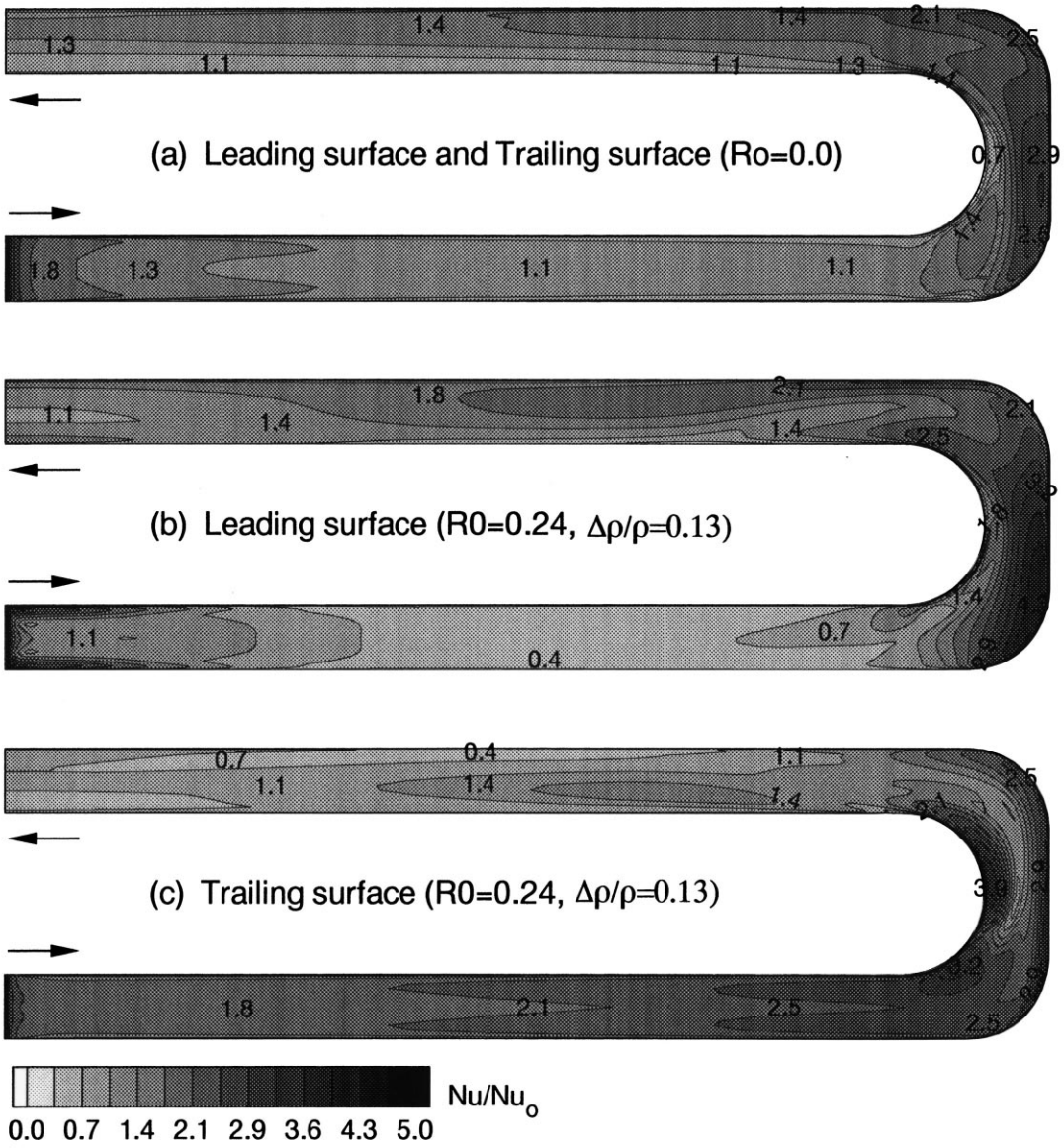

Fig. 5. Detailed Nusselt number distributions; Re = 25,000.

fluids and impingement on the surface as a result of the high pressure gradient in the bend. The Coriolis force in the second passage causes an increase of the leading surface Nusselt number and a decrease of the trailing surface Nusselt number ratio which is opposite to that observed in the first channel. Note that the Coriolis force acts in the opposite direction to that in the first passage when the fluid moves radially inward. Consequently, the cooler fluid is pushed towards the leading surface instead of the trailing surface.

The sharp reduction in heat transfer along the leading surface in the first passage is well predicted in the two-layer calculations. However, the two-layer k–ε model failed to capture the steep increase in heat transfer along the trailing surface in the first passage and in the bend region. On the other hand, the near-wall second-moment solutions are in considerably better agreement with the experimental data on all four side walls. Since both the two-layer and second-moment calculations were performed using the same numerical method and grids, the improved prediction can clearly be attributed to the inclusion of the Reynolds stress anisotropy in the present second-order Reynolds stress closure model. Finally, it should also be noted that the

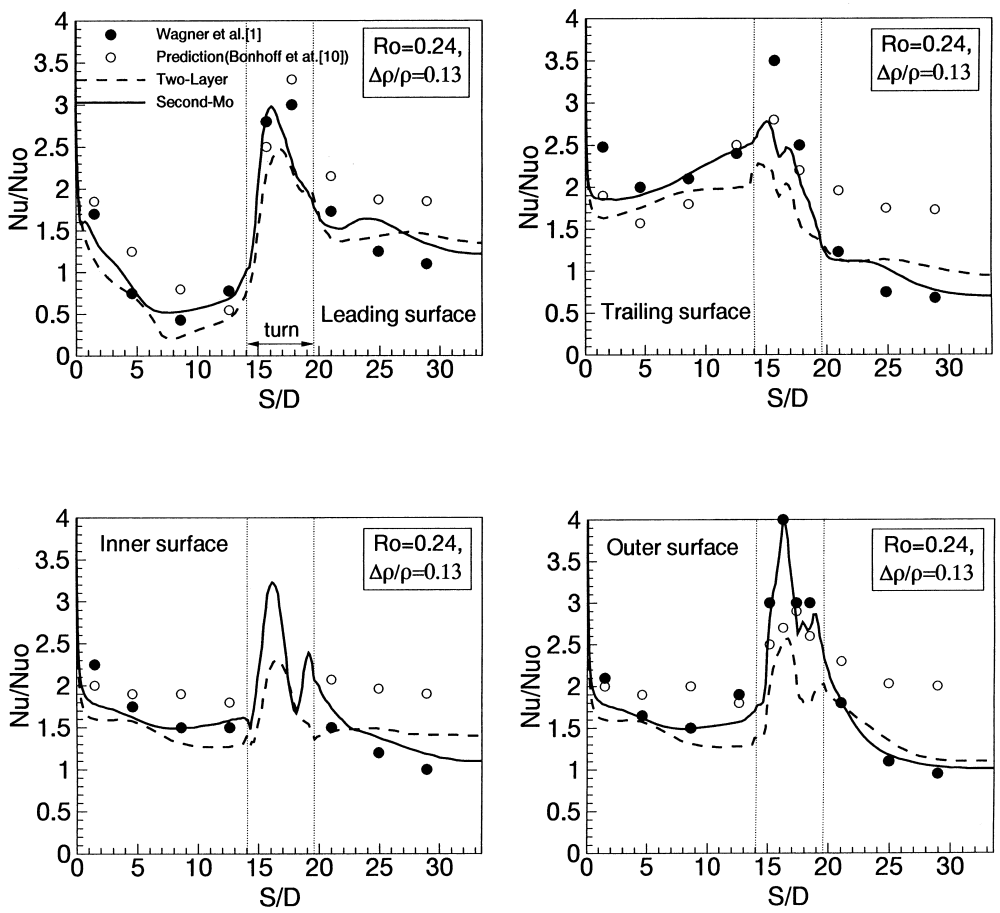

Fig. 6. Calculated and measured Nusselt number ratios; Re = 25,000.

first data point is always higher than the prediction. This might be due to the sudden-contraction entrance conditions in Wagner et al. [1] experiments which differs significantly from the fully-developed flow conditions used in the present calculations. It is also worthwhile to note the present near-wall second-moment model yields considerably more accurate predictions than the Reynolds stress model employed by Bonhoff et al. [10]. The improved predictions may be attributed to the use of more sophisticated SSG second-moment closure in the fully turbulent region as well as the inclusion of the near-wall closure which provides detailed resolution of the laminar sublayer and the buffer layer adjacent to the channel walls.

In order to provide a thorough evaluation of the present second-moment closure model, comparisons have also been made with available data for various combinations of rotation numbers and coolant-to-wall density ratios. Fig. 7 shows the effect of the rotation number on the Nusselt number ratio distribution. The rotation number was varied from 0 to 0.24. The Reynolds number and inlet density ratio were fixed at 25,000 and 0.13, respectively. It is seen that the present second-moment results agree very well with the experimental data of Wagner et al. [1] for all three rotation numbers considered. In general, higher rotation number induces stronger Coriolis and centrifugal buoyancy forces. In the first passage, an increase in rotation number increases the heat transfer on the trailing surface but decreases the heat transfer on the leading surface. In the second passage, the effect of rotation is reversed and considerably weaker than that observed in the first passage. It is also noted that, in general, the heat transfer increases with increasing rotation number on both the inner and outer surfaces.

Fig. 8 shows the effect of coolant-to-wall density ratio on the Nusselt number ratios. The inlet density ratio ($\Delta\rho/\rho$) was varied from 0.07 to 0.22. The Reynolds number and rotation number were held constant at 25,000 and 0.24, respectively. With increasing density ratio, the heat transfer increases greatly on the trailing surface in the first passage. In the second pas-

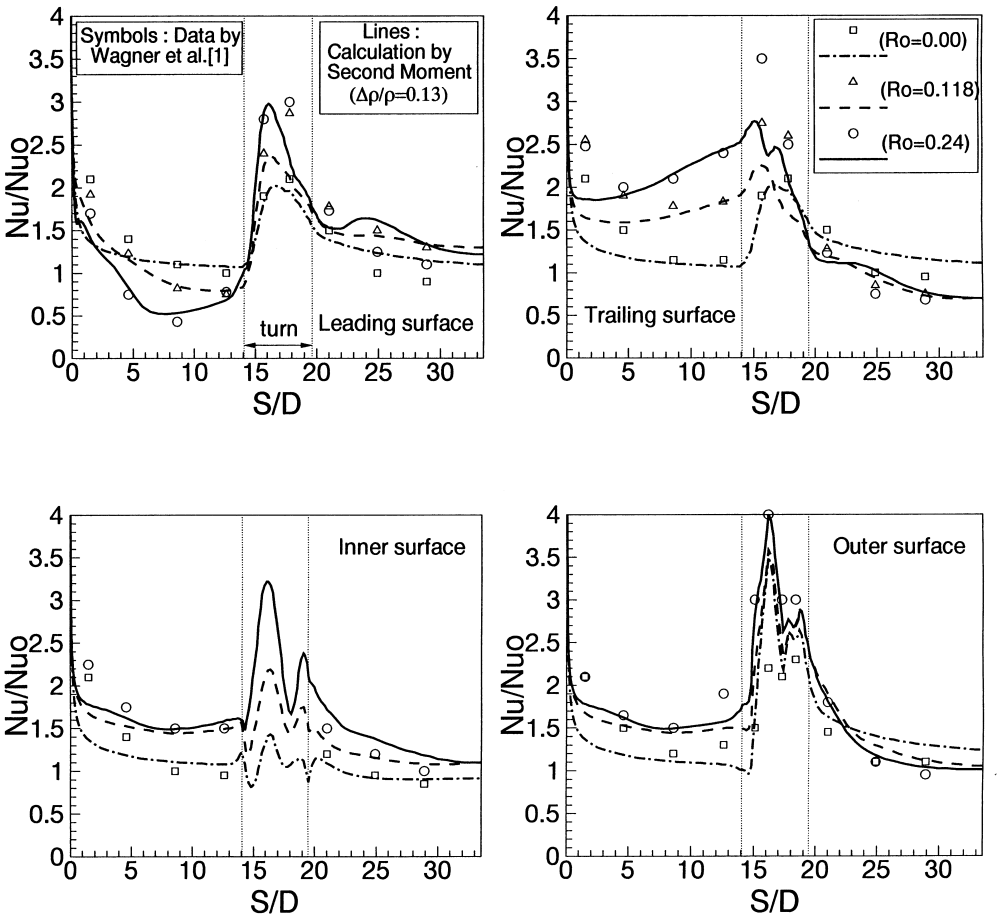

Fig. 7. Effect of rotation on Nusselt number ratios; Re = 25,000.

sage, the heat transfer is not significantly affected by the density ratio. The heat transfer on the inner and outer walls were also found to be fairly insensitive to density ratio. The calculated Nusselt number distributions are in close agreement with the experimental data of Wagner et al. [1] on both the leading and trailing surfaces. The numerical results shown in Figs. 6–8 clearly demonstrated the capability of the present near-wall second-moment closure model for accurate prediction of complex three-dimensional flow and heat transfer characteristics resulting from the rotation and strong wall curvatures.

5. Conclusions

A chimera RANS method was employed for the calculation of three-dimensional flow and heat transfer in rotating two-pass square channels with smooth walls. The method solved Reynolds-averaged Navier–Stokes equations in conjunction with a near-wall second-order Reynolds stress closure model for accurate resolution of the turbulent flow and thermal fields produced by rotation and buoyancy effects. Calculations were also performed using a two-layer isotropic eddy viscosity model to facilitate a detailed assessment of the second-order effects due to the Reynolds stress anisotropy.

For the rotating two-pass square channels considered here, the Coriolis and centrifugal buoyancy forces produced strong nonisotropic turbulence which significantly influenced the development of momentum and thermal boundary layers along the duct. It is therefore important to employ second-moment closure models which solve each individual Reynolds stress component directly from their respective transport equations. The present near-wall second-moment closure model accurately predicted the complex three-dimensional flow and heat transfer characteristics resulting from the rotation and strong wall curvatures. It provides the most reliable numerical predic-

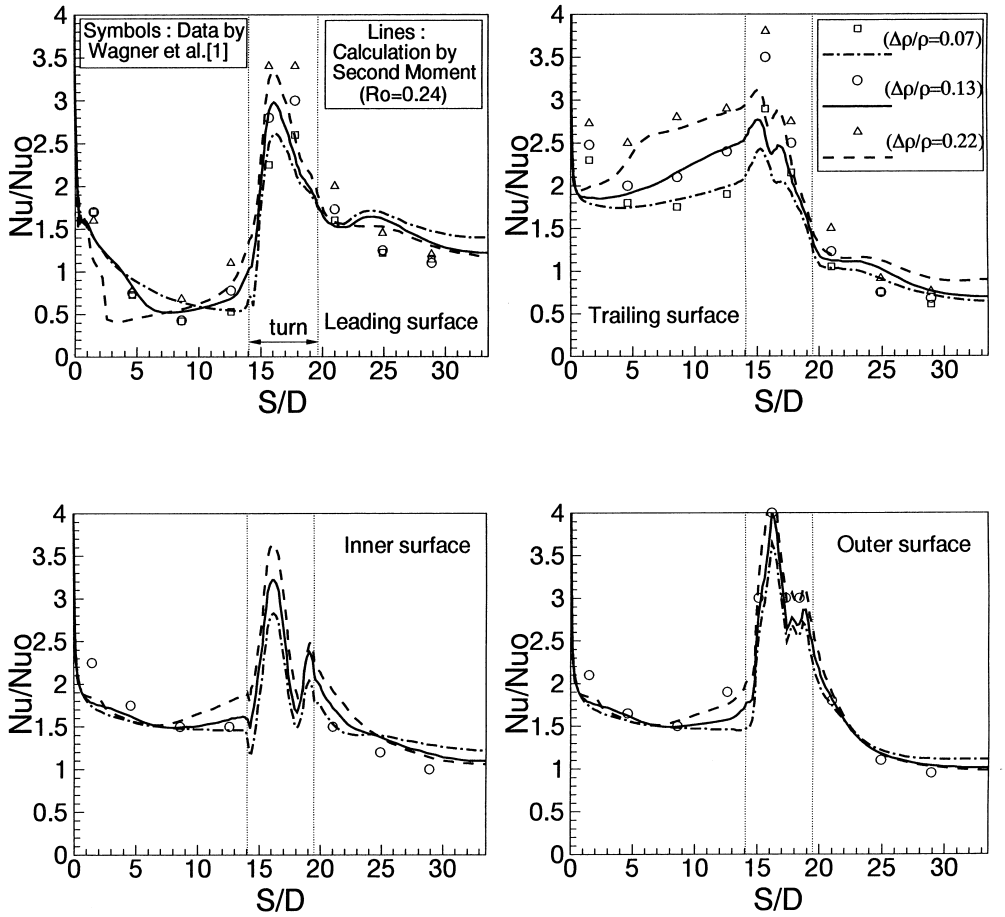

Fig. 8. Effect of coolant-to-wall density ratio on Nusselt number ratios; Re = 25,000.

tions which are in good agreement with the experimental data of Wagner et al. [1].

Acknowledgements

This work was supported by the Texas Higher Education Coordinating Board, Advanced Technology Program, under grant number 999903-165. The computations were performed on the Cray J90 at the Texas A&M Supercomputer Center under a supercomputer research grant and the Cray C90 at Cray Research Inc. in Eagen, Minnesota under the sponsorship of Frank Kampe. Their support is greatly appreciated.

References

[1] J.H. Wagner, B.V. Johnson, F.C. Kopper, Heat transfer in rotating serpentine passage with smooth walls, J. Turbomach. 113 (3) (1991) 321–330.

[2] C. Prakash, R. Zerkle, Prediction of turbulent flow and heat transfer in a radially rotating square duct, J. Turbomach. 114 (4) (1992) 835–846.

[3] T. Bo, H. Iacovides, B.E. Launder, Developing buoyancy-modified turbulent flow in ducts rotating in orthogonal mode, J. Turbomach. 117 (3) (1995) 474–484.

[4] S. Dutta, M.J. Andrews, J.C. Han, Prediction of turbulent heat transfer in rotating smooth square ducts, Int. J. Heat Mass Transfer 39 (12) (1996) 2505–2514.

[5] D.L. Besserman, S. Tanrikut, Comparison of heat transfer measurements with computations for turbulent flow around a 180 degree bend. Paper 91-GT-2, ASME, 1991.

[6] P.S. Sathyamurthy, K.C. Karki, S.V. Patankar, Prediction of turbulent flow and heat transfer in a rotating square duct with a 180 degree bend. Paper 94-GT-197, ASME, 1994.

[7] D.M. McGrath, D.G.N. Tse, A combined experimental/computational study of flow in turbine blade cooling

passage. Part 2. Numerical simulations. Paper 95-GT-149 ASME, 1995.
[8] M.A. Stephens, T.I.P. Shih, K.C. Civinskas, Computations of flow and heat transfer in a rotating U-shaped square duct with smooth walls. Paper No. 96-3161, AIAA, 1996.
[9] H. Iacovides, B.E. Launder, H.Y. Li, The computation of flow development through stationary and rotating U-ducts of strong curvature, Int. J. Heat Fluid Flow 17 (1) (1996) 22–33.
[10] B. Bonhoff, U. Tomm, B.V. Johnson, I. Jennions, Heat transfer predictions for rotating U-shaped coolant channels with skewed ribs and with smooth walls. Paper 97-GT-162, ASME, 1997.
[11] H.C. Chen, Assessment of a Reynolds stress closure model for appendage-Hull junction flows, J. Fluids Eng. 117 (4) (1995) 557–563.
[12] H.C. Chen, Submarine flows studied by second-moment closure, J. Eng. Mech. 121 (10) (1995) 1136–1146.
[13] H.C. Chen, V.C. Patel, Near-wall turbulence models for complex flows including separation, AIAA J. 26 (6) (1988) 641–648.
[14] H.C. Chen, V.C. Patel, S. Ju, Solutions of Reynolds-averaged Navier–Stokes equations for three-dimensional incompressible flows, J. Comput. Phys. 88 (2) (1990) 305–336.
[15] C.G. Speziale, S. Sarkar, T.B. Gatski, Modelling the pressure–strain correlation of turbulence: an invariant dynamical systems approach, J. Fluid Mech. 227 (1991) 245–272.
[16] B.J. Daly, F.H. Harlow, Transport equations in turbulence. Phys. Fluids, (13) (1970) 2634–2649.
[17] B.E. Launder, Second-moment closure: present... and future?, International Journal of Heat and Fluid Flow 10 (4) (1989) 282–300.
[18] D.M. Snider, M.J. Andrews, Rayleigh–Taylor and shear driven mixing with an unstable thermal stratification, Phys. Fluids 6 (10) (1994) 3324–3334.
[19] H.C. Chen, M. Chen, Chimera RANS simulation of a berthing DDG-51 ship in translational and rotational motions, Int. J. Offshore Polar Eng. 8 (3) (1998) 182–191.
[20] C.J. Chen, H.C. Chen, Finite analytic numerical method for unsteady two-dimensional Navier–Stokes equations, J. Comput. Phys. 53 (2) (1984) 209–226.
[21] H.C. Chen, V.C. Patel, The flow around wing-body junctions, in: Proceedings of the 4th Symposium on Numerical and Physical Aspects of Aerodynamic Flows, Long Beach, CA, 1989.
[22] H.C. Chen, R. Korpus, Multi-block finite-analytic Reynolds-averaged Navier–Stokes method for 3D incompressible flows, in: ASME Fluids Engineering Conference 1993, FED-Vol. 150, 1993, pp. 113–121.
[23] B.J. Hubbard, H.C. Chen, A chimera scheme for incompressible viscous flows with applications to submarine hydrodynamics, in: 25th AIAA Fluid Dynamics Conference, Colorado Spring, CO, AIAA, 1994 (Paper 94-2210).
[24] H.C. Chen, E.T. Huang, Validation of a chimera RANS method for transient flows induced by a full-scale berthing ship, in: Proceedings of the 22nd Symposium on Naval Hydrodynamics, Washington, DC, August 9–14, 1998.
[25] H.C. Chen, T. Liu, Turbulent flow induced by a full-scale ship in harbor, J. Eng. Mech. 125 (7) (1999) 827–835.
[26] W.M. Kays, M.E. Crawford, Convective Heat and Mass Transfer, 3rd ed., McGraw-Hill, 1993.
[27] J.P. Steinbrenner, J.R. Chawner, C.L. Fouts, The GRIDGEN 3D Multiple Block Grid Generation System, Vols. I&II, Wright Patterson AFB, OH, 1990 (WRDC-TR-90-3022).